arXiv:1605.05200v1 [astro-ph.SR] 17 May 2016

Termination of the MRI via parasitic instabilities in core-collapse supernovae: influence of numerical methods

T. Rembiasz[1], M. Obergaulinger[1], P. Cerdá-Durán[1], M.Á. Aloy[1] and E. Müller[2]

[1] Departamento de Astronomía y Astrofísica, Universidad de Valencia, C/ Dr. Moliner 50, 46100 Burjassot, Spain

[2] Max-Planck-Institut für Astrophysik, Karl-Schwarzschild-Str. 1, 85748 Garching, Germany

E-mail: martin.obergaulinger@uv.es

Abstract. We study the influence of numerical methods and grid resolution on the termination of the magnetorotational instability (MRI) by means of parasitic instabilities in three-dimensional shearing-disc simulations reproducing typical conditions found in core-collapse supernovae. Whether or not the MRI is able to amplify weak magnetic fields in this context strongly depends, among other factors, on the amplitude at which its growth terminates. The qualitative results of our study do not depend on the numerical scheme. In all our models, MRI termination is caused by Kelvin-Helmholtz instabilities, consistent with theoretical predictions. Quantitatively, however, there are differences, but numerical convergence can be achieved even at relatively low grid resolutions if high-order reconstruction methods are used.

1. Introduction

The iron core of a massive star (zero-age main-sequence mass $M_{\rm ZAMS} \gtrsim 8\,M_\odot$) collapses within a few hundred milliseconds from a radius of a few thousand kilometer and a central density of the order of $\rho_{\rm c} \sim 10^{10}\,{\rm g\,cm^{-3}}$ to a proto-neutron star (PNS) with a radius of $\sim 50\,{\rm km}$ and a central density above nuclear matter saturation density, $\rho_{\rm nuc} \sim 2\times10^{14}\,{\rm g\,cm^{-3}}$. A hydrodynamic shock wave forms when the core bounces because of the stiffness of nuclear matter. This prompt shock stalls because of severe energy losses due to photo-disintegration of heavy nuclei into free nucleons, and turns into an accretion shock initially located at a radius $\sim 100\,{\rm km}$, through which matter continues to accrete onto the PNS. Most of the gravitational binding energy liberated during the collapse is radiated away in the form of neutrinos. A small fraction of these neutrinos inteact with matter in the post-shock layers depositing energy, which revive the stalled shock and eventually cause a core-collapse supernova explosion (CCSN). A failure to revive the shock before accretion increases the mass of the PNS beyond the maximum mass that can be supported against gravity, will lead to a secondary collapse to a black hole. Hence, the fate of the core hinges on the efficiency of the energy transfer to the post-shock matter, which may be enhanced by various hydrodynamic instabilities (convection and the standing accretion shock instability, SASI). The exact conditions for the neutrino-driven explosion mechanism to launch an explosion of the star compatible with the observations (in particular concering the explosion energy) is currently a matter of intense investigation (for a review see, e.g., [1], [2], [3], [5]).

If the pre-collapse core rotates rapidly, part of its rotational energy might be tapped to aid the neutrino-driven mechanism. The efficiency of this effect is greatly enhanced in strongly magnetised cores. However, the presence of both rapid rotation and strong fields is unlikely except for possibly a very small set of progenitors. Therefore, assuming a rapidly rotating core, the prospects for rotationally aided or even rotationally driven explosions greatly increase if strong magnetic stresses can be generated after collapse, i.e. if a weak seed field is efficiently amplified during the time before either an explosion is launched by other mechanisms or the PNS collapses to a black hole.

Angular momentum conservation during collapse causes the core to speed up and strong differential rotation is generated at the edge of the homologously collapsing inner core, even for initially rigidly rotating iron cores. This opens additional channels for the amplification of seed fields besides flux conservation in the (compressive) accretion flow and a possible turbulent dynamo driven by hydrodynamic instabilities that do not rely on rotation. Winding of a pre-existing poloidal field component creates a toroidal component that grows linearly with time (e.g. [6]). Possibly more important still, a significant fraction of the core fulfils the instability criterion for the magneto-rotational instability (MRI) [7]. In its most basic form, MRI requires a negative radial gradient of the angular velocity, $\partial_r \Omega < 0$, and a weak background field to increase field perturbations on an exponential timescale. The growth time of the instability is comparable to the rotational period of the core that can be much shorter than the post-collapse evolution timescale ($\sim 100\,\mathrm{ms}$).

The MRI has been intensively studied in the context of accretion discs, where it is considered to provide the most important source of turbulence and enhanced angular-momentum transport [8]. In CCSN, indications for its activity have been found in global axisymmetric simulations [9, 10, 11, 12]. Furthermore, it has been investigated in local shearing box simulations [13, 15]. Both types of models suggest that the MRI can indeed grow under conditions typical for PNS. So far, these studies leave, however, several questions open, most importantly what is the amplitude of the turbulent stress generated by the MRI. In a new set of simulations, we focus on the transition from the initial phase of exponential growth of the MRI to turbulence. In the former phase, the MRI takes the form of laminar *channel modes*, pairs of radial inflows and outflows containing magnetic fields of opposite polarity. They contain shear layers as well as current sheets, which can become unstable against Kelvin-Helmholtz (KH) instabilities or tearing-modes (TM). The growth rate of these secondary, *parasitic* instabilities is proportional to the radial component of the velocity or magnetic field, respectively. Since these components grow exponentially at a constant rate, γ_{MRI}, the growth rate of the parasitic instabilities increases exponentially with time and, consequently, their amplitude grows super-exponentially. When the amplitudes of the parasites are as large as the amplitude of the MRI itself, they terminate the MRI growth, initiating the saturation phase. This parasitic termination scenario was described by [16] and analysed in detail by [17], who determined the growth rate of the KH instabilities and TM, and identified which of the two parasites should dominate given the viscosity and resistivity of the gas.

To test the predictions of [17] under conditions representative for the outer layers of a differentially rotating PNS, we performed a set of local three-dimensional simulations of the MRI in the shearing-disc approach ([18, 13]) varying the viscosity and resistivity. For a detailed discussion of our simulations, see [19]. Here, we will focus on the impact that different numerical methods have on the results.

2. Setup and numerical methods

We solve the equations of visco-resistive MHD in the presence of an external gravitational field and use the same initial and boundary conditions as in [19]. The simulation domain covers 1 km to 4 km in each direction of a cylindrical box (r, z, ϕ) centered at a radius of $r_0 = 15.5\,\mathrm{km}$. The

name	reco.	reso.	box	$\gamma_{\rm MRI}$ [$\rm s^{-1}$]	$\mathcal{M}_{r\phi}^{\rm term}$ [10^{30} $\rm G^2$]
PLM-8	PLM	8	s	926	2.2
PLM-10	PLM	10	s	959	2.3
PLM-16	PLM	16	s	1089	1.9
PLM-20	PLM	20	l	1116	1.9
PLM-34	PLM	34	s	1123	1.8
MP5-8	MP5	8	s	1093	1.1
MP5-10	MP5	10	s	1104	1.4
MP5-16	MP5	16	s	1127	1.1
MP5-20	MP5	20	s	1134	0.85
MP5-34	MP5	34	s	1127	1.0
MP9-8	MP9	8	s	1104	0.79
MP9-10	MP9	10	s	1122	1.3
MP9-16	MP9	16	s	1130	1.1
MP9-20	MP9	20	l	1126	1.1
MP9-25	MP9	25	l	1127	1.0
MP9-34	MP9	34	s	1127	0.93
MP9-67	MP9	67	l	1127	0.73
MP9-134	MP9	134	s	1128	0.73

Table 1. List of models. The first column displays the name of the model, which is a combination of the reconstruction method ($2^{\rm nd}$ column) and the grid resolution, measured in grid cells per MRI wavelength ($3^{\rm rd}$ column). In the $4^{\rm th}$ column, letters indicate the size of the simulation domain: 's' (small) and 'l' (large) stand for box sizes of $1\,\rm km \times 1\,km \times 0.333\,km$ and $1\,\rm km \times 4\,km \times 1\,km$, respectively. The last two columns give the growth rate of the MRI and the termination value of the Maxwell stress (defined in Eq. 2), respectively.

initial profiles of gravitational potential, density, and pressure are derived from the post-bounce state of the global simulations of [9]. In addition, we assume an angular velocity with a simple power law profile,

$$\Omega = \Omega_0 \left(\frac{r}{r_0}\right)^{-q}, \tag{1}$$

where $q = 1.25$, and $\Omega_0 = 1824\,\rm s^{-1}$. This profile is hydrodynamically stable.

If we add a uniform magnetic field in z-direction, the MRI will grow from small perturbations. The geometry and strength of the CCSN cores our models are supposed to represent depends on the pre-collapse fields as well as the evolution during and immediately after collapse and, as a result, are quite uncertain. Stellar-evolution models support a combination of poloidal and toroidal components [4]. Both kinds of fields are susceptible to the MRI. We focus here on the case of a poloidal, in our case vertical, field because the MRI grows fastest for this field component. By focusing on a uniform field, we furthermore neglect possible small-scale structures, which might yield small corrections to the geometry, but not the growth rate of the MRI.

We impose periodic boundary conditions in z and ϕ direction, and shearing-disc boundaries in radial direction, i.e. boundaries that are periodic in the deviation of the hydrodynamic variables from the initial (background) state.

The parameters of our simulations are based on the models of [19]. The theoretical growth rate of the MRI is $\gamma_{\rm MRI} = q\Omega_0/2 \approx 1140\,\rm s^{-1}$. We use an initial magnetic field of $b_0^z = 4.6 \times 10^{13}\,\rm G$, corresponding to $\lambda_{\rm MRI} \approx 333\,\rm m$. We neglect viscosity and use a uniform resistivity $\eta = 4.45 \times 10^8\,\rm cm\,s^{-1}$. The most important parameter that, as we will show below,

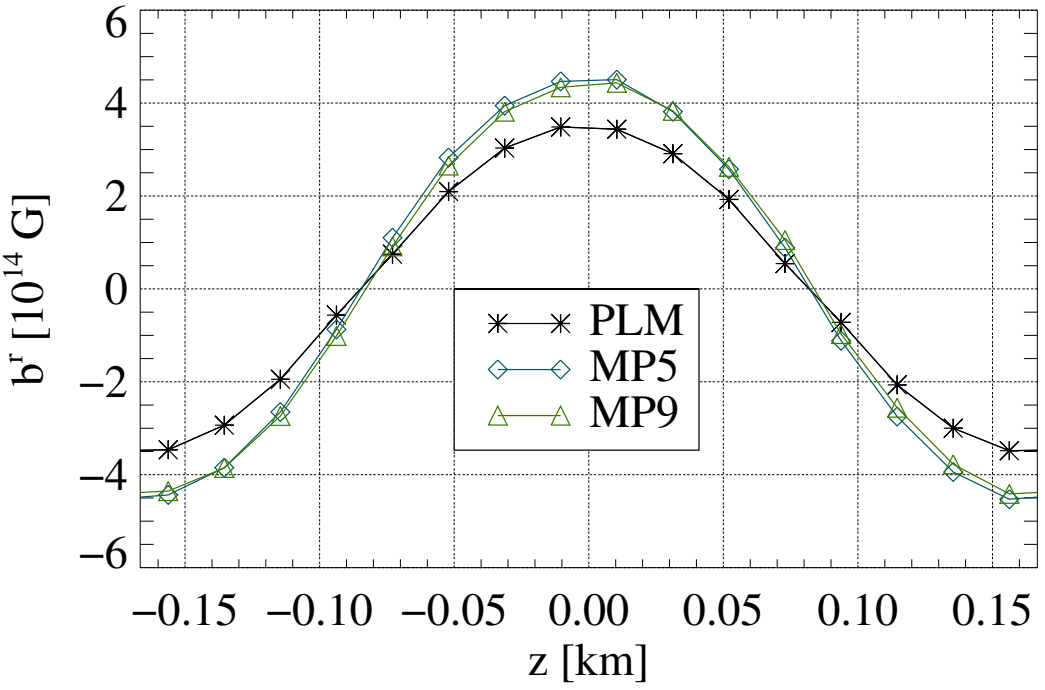

Figure 1. Vertical profiles of the radially averaged radial magnetic field at $t = 10\,\mathrm{ms}$ for models PLM-16, MP5-16, and MP9-16.

causes differences between the simulations is the grid resolution, which we express in terms of the number of grid cells per channel width. We present our set of models in Tab. 1. We point out that our simulation results are scalable to different values of r_0, Ω_0, and b_0^z (see, [19]).

Our numerical code is based on a dimensionally unsplit finite-volume discretisation of the MHD equations and the constrained-transport scheme to ensure a divergence-free evolution of the magnetic field. The spatial reconstruction can be done using the following methods:

- piecewise-constant reconstruction of 1^{st}order;
- TVD piecewise-linear (PLM) reconstruction (2^{nd}order) with several slope limiters;
- 4^{th}-order WENO reconstruction;
- monotonicity-preserving reconstruction (MP; [20]) of 3^{rd}, 5^{th}, 7^{th}, or 9^{th} order.

In [19], we used the most accurate of these schemes, viz. 9^{th}-order MP reconstruction. Here, we will make a comparison to two methods of lower order: 5^{th}-order MP, and PLM with the MC slope limiter. The other ingredients of the code are the same as in [19]: a multi-stage (MUSTA) version of the HLLD Riemann solver and a 3^{rd}-order Runge-Kutta time integrator.

3. Results

For the conditions in supernova cores, [19] found, as predicted by [17], that the MRI growth is terminated by KH modes, unless special conditions such as an insufficient size of the numerical domain somewhat artificially restrict their growth. This qualitative finding also holds for less accurate reconstruction schemes.

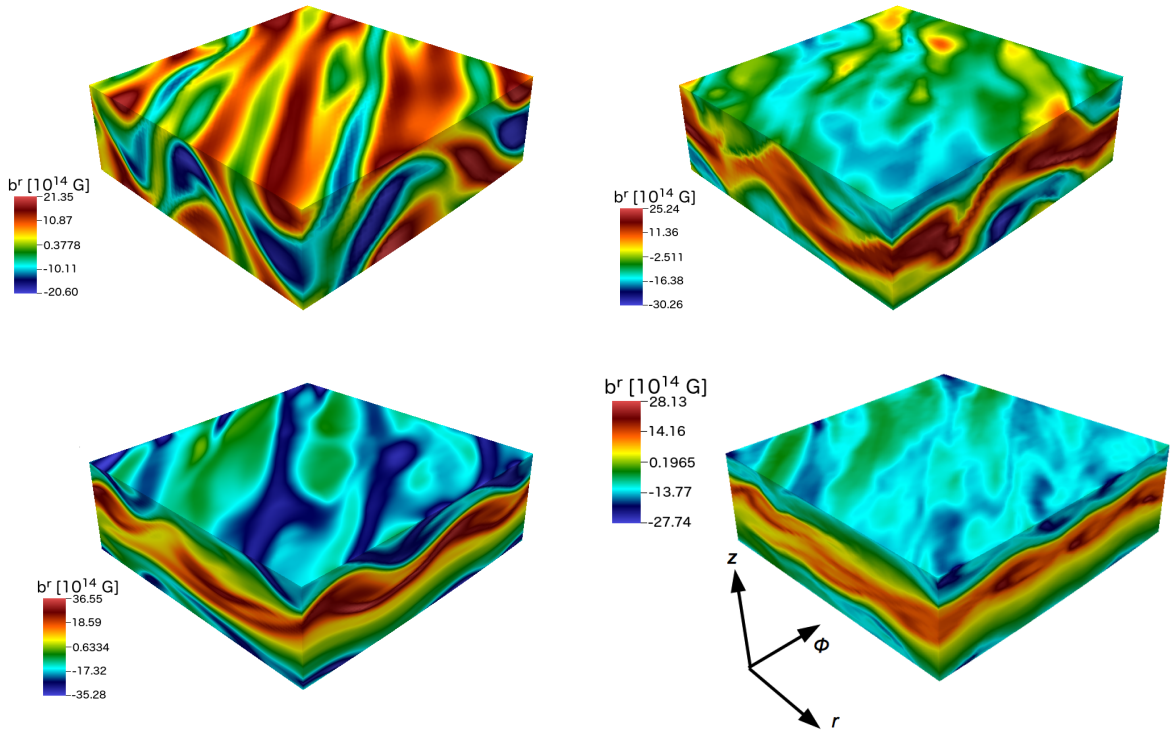

Figure 2. Visualisation of the radial component of the magnetic field close to the moment of termination for models (top left to bottom right) PLM-16 (at $t = 12\,\mathrm{ms}$), MP9-16 (at $t = 11.5\,\mathrm{ms}$), PLM-34 (at $t = 11.5\,\mathrm{ms}$), and MP9-34 (at $t = 11\,\mathrm{ms}$), respectively. Note that not all snapshots are taken at the same evolutionary time, but they correspond to the same evolutionary instant, namely the time at which (for each model) saturation of the MRI growth sets in.

Irrespective of the reconstruction method, MRI channel modes start to grow from the weak perturbations introduced at $t = 0$. Even for low grid resolution and low-order schemes, the vertical profiles that we find in the simulations approximate very well sine functions, as we show for the radial component of the magnetic field of models PLM-16, MP5-16, and MP9-16 in Fig. 1. The numerical growth rates of the MRI depend on the resolution and the reconstruction scheme. Under-resolved simulations show in general a slower MRI growth, but as the grid resolution increases, all methods exhibit numerical convergence to the theoretical value. The good agreement between numerical schemes shown in Fig. 1 holds well throughout the exponential growth phase. Differences show up when the growth is terminated, leading to a spread in the value of the termination amplitude (see below).

The channel modes constitute the background in which parasitic instabilities grow. We compare visualisations of the radial component of the magnetic field for models with PLM and MP9 reconstruction schemes and two resolutions in Fig. 2. We note that the snapshots show a very dynamical phase of the evolution, during which a slight time difference corresponds to a very pronounced difference in the state of the flow. Therefore (and because of the influence of random perturbations), a point-wise comparison between the four panels cannot be made. Nevertheless, we conclude that the parasites have the same structure as the one found in [19], and thus can be identified as KH instabilities. In particular, patterns such as the vortices visible in the r–z-planes of the lower two panels provide evidence for KH modes. The rather different appearance of the two upper panels (with a resolution of 16 zones per channel) is not caused

by a difference in the parasites, but is a consequence of the fact that the parasites have grown somewhat more than in the two bottom panels.

Analogously to MRI channels, KH modes grow at a reduced rate if the numerical resolution is insufficient. This means that, for the same MRI amplitude, the KH parasites grow slower. Consequently, the time at which the parasites are strong enough to terminate the MRI growth is delayed for a coarse grid. Furthermore, KH parasite modes develop structures smaller than the channel mode. Therefore, insufficient resolution affects them more than the MRI, and parasitic modes can be suppressed on a grid where the MRI growth rate is hardly reduced. Thus, non-converged simulations tend to *overestimate* the termination amplitude of the MRI as measured by, e.g. the maximum value of the volume-averaged Maxwell stress component,

$$\mathcal{M}_{r\phi} = \frac{|\int b^r b^\phi \mathrm{d}V|}{V}, \tag{2}$$

where V is the total grid volume. This tendency is ameliorated for more accurate numerical schemes.

We summarise the results described above in Fig. 3. The three top panels show the time evolution of $\mathcal{M}_{r\phi}$ for simulations with resolutions of 8, 16, and 34 zones per channel. Except at the lowest resolution, for which the PLM run exhibits a low growth rate, the exponential MRI growth is captured well. Comparing the growth rates for all simulations (bottom left panel), we can quantify the differences between the reconstruction methods: PLM requires roughly 34 zones per channel to attain a growth rate $\gamma_{\mathrm{MRI}} > 1120\,\mathrm{s}^{-1}$, whereas the MP schemes achieve that value already at 16 (MP5) and 10 (MP9) zones, respectively.

In the top panels, MRI termination corresponds to the maximum value of $\mathcal{M}_{r\phi}(t)$. The bottom right panel compares this maximum for all models. Because of the suppression of the growth of the parasites at low resolutions, the termination amplitude increases with resolution until a sufficiently large number of zones per channel width is reached. Then it settles to a roughly constant value. Please note that the runs with 8 zones per channel represent a special case for which other effects beside parasitic KH modes affect termination such as the diffusion of magnetic field and momentum across the current and shear layers, respectively. Furthermore, model MP5-20 deviates from the trend, possibly indicating the range of stochastic variations of the termination amplitude. We find considerable differences between PLM and the two MP schemes, with the former yielding an almost twice as high $\mathcal{M}_{r\phi}^{\mathrm{term}}$ as the two other at the same resolution. Restrictions in computing time allowed us to obtain numerical convergence only for the MP9 models, which approach a value of $\mathcal{M}_{r\phi}^{\mathrm{term}} = 0.73 \times 10^{30}\,\mathrm{G}^2$, if we use at least 67 zones per channel. We expect, however, the other models to behave similarly for a sufficiently high grid resolution.

4. Summary and conclusions

In an extension of the studies of [13] and [19], we investigated the influence of numerical effects on the early evolution of the MRI in conditions similar to those expected in core-collapse supernovae. We performed a series of three-dimensional MHD simulations in the shearing-disc framework, fixing the physical conditions (rotational profile, density, initial field) in such a way that we could observe the growth of MRI channel modes and their disruption by parasitic Kelvin-Helmholtz modes and varying the grid resolution and the reconstruction method. For the latter, we used a 2^{nd} order piecewise linear reconstruction with the MC slope limiter, as well as monotonicity-preserving methods of 5^{th} and 9^{th} order accuracy.

The main results of this study are the following:

- The physical nature of the parasitic instability terminating the MRI does not depend on the numerical settings. The structure of the flow and the field show the signatures of KH modes, which are consistent with the theoretical predictions of [17].

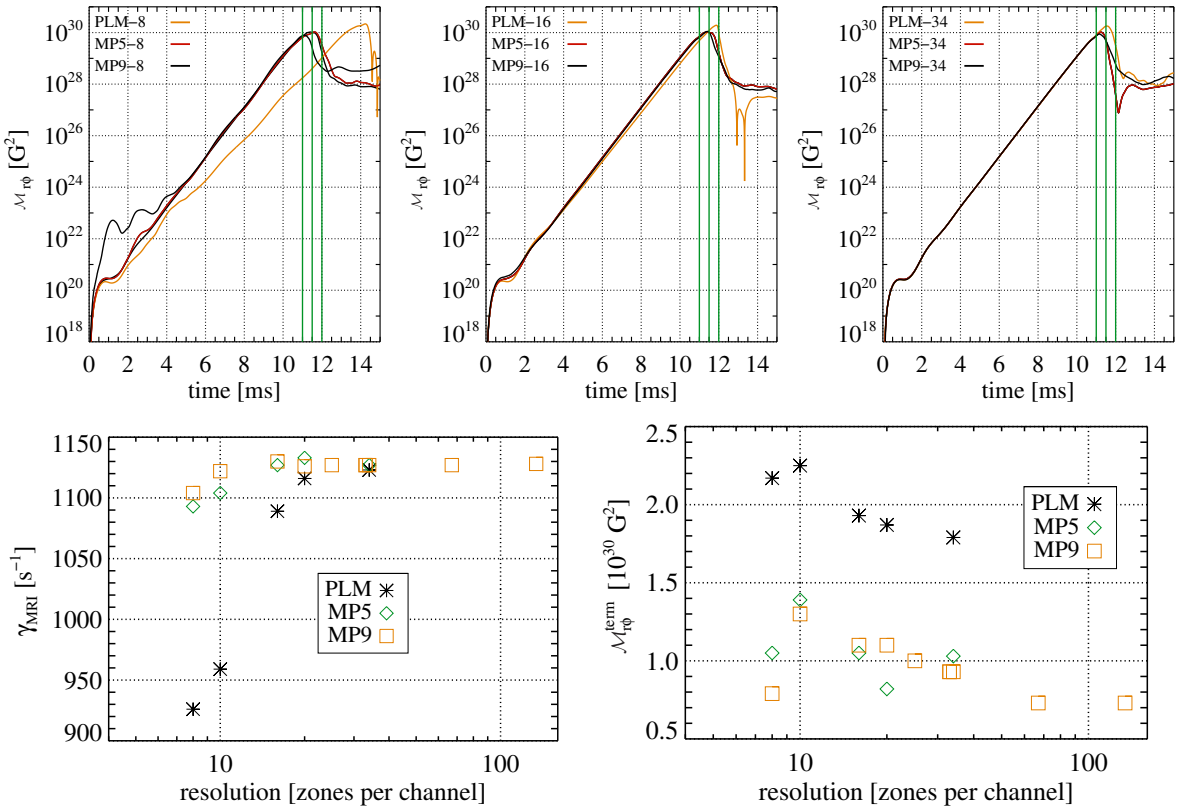

Figure 3. Top panels: time evolution of $\mathcal{M}_{r\phi}$ for models with grid resolutions of 8, 16, and 34 zones per channel (left to right). Bottom panels: dependence of the growth rate (left) and the termination amplitude (right) of the MRI on the grid resolution.

- All methods capture the exponential growth of the MRI well at low resolution of the order of 10 zones per channel, with MP schemes performing better than PLM.
- The termination value of the Maxwell stress exhibits convergence with grid resolution. Under-resolved simulations overestimate its value because numerical viscosity reduces the growth rate of the parasites. Again, MP schemes are superior to PLM. In general, a much higher resolution is required to obtain the correct parasitic growth rate than that of the MRI itself, because KH modes grow on much smaller length scale, viz. the extent of the shear layer between the channel flows.

From these results we conclude that the most important findings concerning the MRI termination are robust w.r.t. the effects of numerical schemes, which affirms our previous studies. Our initial field strengths, and thus the MRI wave lengths, most likely exceed those that can be expected in most supernova cores (the post-collapse fields of [14] would, in a rapidly rotating core, correspond to $\lambda_{\rm MRI} \sim 0.01...10\,$m). This means that for realistic initial fields, the constraint to resolve the KH instability in the shear layer can translate into a very severe restriction on the grid resolution beyond what can be currently afforded in global models. Simulations that cannot meet this resolution requirement run the risk of producing too high amplitudes of the MRI at termination, which may lead to unphysically strong magnetic stresses and consequently tend to overestimate the influence of magnetic fields on the dynamics. Although the use of high-order methods, such as our MP5 and MP9 schemes, does not overcome this limitation, at least it helps to alleviate it. We estimate that a three-dimensional simulation with a high-order method following the evolution for a time scale of $\sim 100\,$ms and resolving channels of 1 m length scale in

a PNS of radius 30 km requires $\sim 10^8$ grid cells and $\sim 10^{14}$ CPU hours. Even if adaptive mesh refinement (AMR) techniques were employed, the simulations would still be beyond current possibilities.

Acknowledgments
TR acknowledges support from The International Max Planck Research School on Astrophysics at the Ludwig Maximilian University Munich, EM & TM acknowledge support from the Max-Planck-Princeton Center for Plasma Physics, and MA, PCD, TR and MO acknowledge support from the European Research Council (grant CAMAP-259276). We also acknowledge support from grants AYA2013-40979-P and PROMETEOII/2014-069. The computations have been performed at the Leibniz Supercomputing Center of the Bavarian Academy of Sciences and Humanities (LRZ), the Max Planck Computing & Data Facility (MPCDF), and at the Servei d'Informàtica of the University of Valencia.

References

[1] Mezzacappa, A. et al. 2005, Annual Review of Nuclear and Particle Systems, vol. 55, 467
[2] Janka, H.-T. 2012, Annual Review of Nuclear and Particle Science, 62, 407
[3] Kotake, K. et al. 2012, Advances in Astronomy, vol. 2012, id. 428757
[4] Braithwaite, J., Nordlund, Å., 2006, A&A, 450, 1077
[5] Burrows, A. 2013, Reviews of Modern Physics, 85, 245
[6] Meier, D. L., Epstein, R. I., Arnett, W. D., & Schramm, D. N. 1976, ApJ, 204, 869
[7] Akiyama, S., Wheeler, J. C., Meier, D. L., & Lichtenstadt, I. 2003, ApJ, 584, 954
[8] Balbus, S. A. & Hawley, J. F. 1998, Reviews of Modern Physics, 70, 1
[9] Obergaulinger, M., Aloy, M. A., Dimmelmeier, H., & Müller, E. 2006, A&A, 457, 209
[10] Cerdá-Durán, P., Font, J. A., Antón, L., Müller, E. 2008, A&A, 492, 937
[11] Sawai, H., Yamada, S., & Suzuki, H. 2013, ApJL, 770, L19
[12] Sawai, H., & Yamada, S. 2015, arXiv:1504.03035
[13] Obergaulinger, M., Cerdá-Durán, P., Müller, E., & Aloy, M. A. 2009, A&A, 498, 241
[14] Obergaulinger, M., Janka, H.-Th., Aloy, M.Á, 2014, MNRAS, 445, 3169
[15] Masada, Y., Takiwaki, T., Kotake, K., & Sano, T. 2012, ApJ, 759, 110
[16] Goodman, J. & Xu, G. 1994, ApJ, 432, 213
[17] Pessah, M. E. 2010, ApJ, 716, 1012
[18] Klahr, H. H. & Bodenheimer, P. 2003, ApJ, 582, 869
[19] Rembiasz, T., Obergaulinger, M., Cerdá-Durán, P., Müller, E., & Aloy, M. A., 2016, MNRAS, 456, 3782
[20] Suresh, A. & Huynh, H. 1997, J. Comput. Phys., 136, 83